Optimizing PID Controller Design for Rotor Systems Suspended by Active Magnetic Bearings

I. Abubakar [1] A. Putkonen [1] M. Rehtla [1] T. Lindh [1] S. Derammelaere [2] N.Nevaranta [1]

[1] Department of Electrical Engineering, Lappeenranta University of Technology, FI-53851 Lappeenranta, Finland. E-mail: {Ibrahim.Abubakar,Atte.Putkonen,Marek.Rethla,Niko.Nevaranta,Tuomo.Lindh @lut.fi

[2] Department of Electromechanics, University of Antwerp, Groenenborgerlaan 171 2020 Antwerpen, Belgium. E-mail: Stijn.Derammelaere@uantwerpen.be

Abstract

In many industrial applications, one of the primary advantages of using PID-based controllers is their simplicity, tunability, and ease of implementation. However, in the case of high-speed machines with magnetically suspended rotor systems, the stabilizing control solution often involves combining PID controllers with supporting filter structures. Depending on the case, this can lead to controllers with a significant number of tunable parameters, ranging from 10 to 35, which can be a challenging task when done manually. Therefore, a multiobjective genetic algorithm optimization is proposed in this paper to seek an optimal configuration for the controller parameters. This paper concentrates on optimizing PID-based controllers for AMB-suspended rotor systems, aiming to enable the analysis of outcomes within a standardized framework. Thus, the closed-loop performance is evaluated by the obtained damping properties and robustness. Moreover, an experimental AMB–rotor system is used to assess the performance of the controllers.

Keywords: Active Magnetic Bearing (AMB), PID control, Multiobjective optimization

1 Introduction

The use of high-speed machine technology based on active magnetic bearings (AMBs) is increasing as a result of the general trend toward enhancing both the efficiency and energy density. Such machinery requires closed-loop control solutions to regulate the suspension system that is based on the rotor displacement feedback information. In general, the control solutions can be categorized into model-based solutions like robust H_∞ controllers Sahinkaya and Sawicki (2020), Noshadi et al. (2016), state–space pole placement Nevaranta et al. (2020), or linear quadratic regulators (LQR) Jastrzebski et al. (2019), Hutterer and Schroedl (2022) and decentralized/centralized PID-based solutions Hutterer and Schrödl (2023). The intuitive nature of the tuning process and diagnosis often favors PID-based solutions; however, in the context of AMB-suspended rotor systems, tuning a PID controller is more challenging because of the necessity of additional filter structures, which adds complexity to the tuning process.

The PID-based control solutions used in an AMB–rotor system will be more complex depending on the rotor dynamics (e.g., several flexible modes to be stabilized and damped, a highly gyrosgopic machine), and therefore, a PID controller with additional filter structures like notch, lead–lag, and low-pass filters are often required to achieve robust stability and performance of an AMB system Wei and Söffker (2016). With such structures, the manual tuning of several control parameters requires engineering experience supported with visual tools Lantto (1999), Polajzer et al. (2016).However, incorporating an optimization algorithm in the
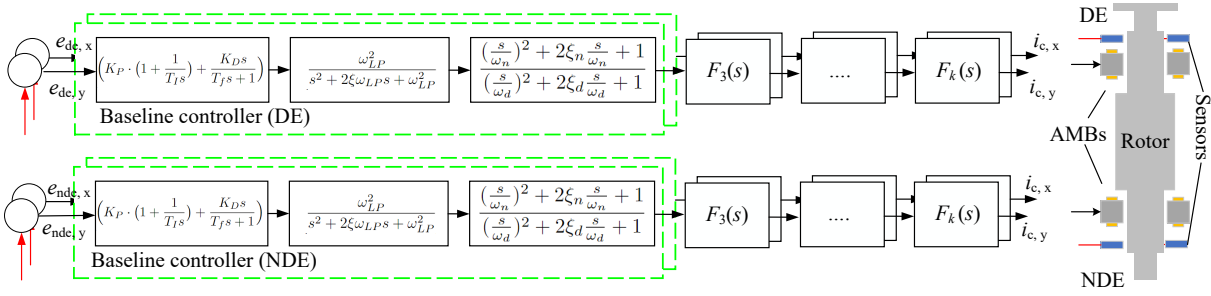
Figure 1: General representation of a stabilizing PID-based controller for AMB-suspended high-speed machines, from the error signal to the control current, where the baseline controller is combined with supporting filters. The label DE indicates the driven end, and NDE represents the nondriven end. The marking e is the error signal for the controllers.

control design will relax the tuning problem Schmied and Kosenkov (2013), Liu et al. (2016).

This paper focuses on the multiobjective optimization problem of tuning PID-based controllers for AMB-suspended high-speed machines. Similar optimization problems for PID-controlled AMB-suspended machines have been investigated in previous research. The optimization problem typically involves dealing with more than one objective to be optimized simultaneously, and thus, multiobjective optimization is applied because it can provide a set of optimal solutions, also known as Pareto optimal solutions Agees Kumar and Kesavan Nair (2011). When considering simple PID-tuning cases in the literature, such as Gaidhane et al. (2017) and Meng and Xue (2009), a multiobjective optimization technique nondominated sorting genetic algorithm (NSGA-II) was considered in the optimization of fractional-order proportional integral derivative (FOPID) controller parameters. In contrast, in Schmied and Kosenkov (2013), the parameters of a PID controller for AMB–rotor systems were numerically optimized using a gradient-based interior point algorithm. However, these papers do not address the stabilization of any flexible modes.

Depending on the complexity of the AMB–rotor system under study, filters can lead to PID-type controllers with a significant number of tunable parameters, typically ranging from 10 to 35. In Liu et al. (2016), a multiobjective genetic algorithm (MOGA) was proposed to optimize a control structure with 34 parameters, where the optimization objectives included output sensitivity, a stable margin at critical speeds, and reducing the controller gain. In Wei and Söffker (2016), two PID controllers were optimized using MOGA considering 30 parameters. The optimization process involved combining both frequency and time domain-based optimization for the evaluation of the fitness function. In Wei and Söffker (2012a), Wei

and Söffker (2012b), Wei (2015), the multiobjective optimization for optimizing a PID controller for an AMB-suspended rotor system was proposed with several time and frequency-domain objectives to be met. Finally, it is noteworthy that multiobjective optimization has also been applied to model-based solutions, particularly for H_∞-based approaches Zhang et al. (2017), Jastrzebski et al. (2010), focusing on optimizing the weighting functions to synthesize the controller that meets the given objectives.

However, despite achieving solid results in the literature covering AMB PID controller optimization problems, it appears that the performance of the controllers is not evaluated within a framework that allows assessing the improvements obtained through the optimization routine. The approach presented here is different from Wei and Söffker (2016), Schmied and Kosenkov (2013), Liu et al. (2016), Wei and Söffker (2012a), Wei and Söffker (2012b), Wei (2015) in several respects. First, the primary focus of this paper is on the multiobjective optimization of PID parameters with the objective of achieving high damping for the flexible modes close to the operating region and minimizing output sensitivity. This approach differs from the existing ones, Wei (2015), that consider several frequency-domain and time-domain objectives, which often lead to difficult trade-offs, Pareto front complexity, solution diversity, and objective prioritization. Additionally, the initial tuning process and the resulting closed-loop outcomes of the existing approaches have not been evaluated experimentally or analyzed using tools to validate their practical applicability, Liu et al. (2016). To establish the validity of manual tuning as a starting point, the initial tuning methodology relies on the Nyquist template proposed in Lantto (1999), which provides a visualization of the loop shaping (tuning) process. The uniqueness of the proposed approach lies in evaluating the optimal controllers against the

initial controller by using various visualization tools. They include generalized Nyquist diagrams with numerical ranges of uncertainty, MIMO closed-loop metrics (incorporating disk margins Seiler et al. (2020)), and an analysis of damping properties with damping ratios. Furthermore, the selected candidate controllers are assessed on experimental AMB-suspended machinery, both in the time and frequency domains. This comprehensive evaluation distinguishes our approach from others Schmied and Kosenkov (2013),Liu et al. (2016),Wei (2015) by providing a thorough understanding of controller performance using different metrics for stability and performance.

This paper is organized as follows: Section 2 focuses on PID-based controller tuning for AMB-suspended rotor systems. Section 3 introduces the optimization problem and focuses on the optimization results. Section 4 provides the experimental results, and Section 5 concludes the paper.

2 PID-based control of AMB-suspended rotors

When considering a rotor system with flexible modes, often a standard PID-type control alone is not able to stabilize the system Liu et al. (2016). Therefore, the complexity of the control system increases as a combination of filters is required to stabilize the flexible modes, resulting in a higher control order. Thus, the control law will be PID combined with a k number of filters expressed in a following general form

$$C(s) = C_{PID}(s) \cdot \prod_{i=1}^{k} F_i(s), \qquad (1)$$

where $C_{PID}(s)$ is the PID controller and $F_i(s)$ is the ith filter structure. Naturally, separate controllers must be designed for both ends of the machine, i.e., in the case of a system with one impeller, for the driven end (DE) for the loaded side and for the nondriven end (NDE) for the opposite end. Based on the literature, it can be justified that for most subcritical and low gyroscopic cases, a controller that combines PID, a second-order low-pass filter, and a second-order lead–lag element is sufficient to stabilize the system Hutterer et al. (2015). Based on the notations in Table 1, this controller already has ten tuning parameters to be selected manually and is represented as $C(s) = C_{PID}(s) \cdot F_2(s) \cdot F_4(s)$. This combination can be considered a baseline controller that can be further enhanced by adding additional filters as depicted in Fig. 1. Naturally, the combination of the controller blocks depends on the machine case under study, but a combination can lead to an extensive number of parameters

Table 1: Typical filter structures in AMB control and their description Wei and Söffker (2016). ω_{LP} is the cutoff frequency and ξ_{LP} is the damping ratio of the low-pass filter. ω_n, ω_d, and ω_a are the natural frequencies of the respective filters, and ξ_n, ξ_d, and ξ_a are their damping ratios.

Filter Number	Structure	Description
$F_1(s)$	$\dfrac{1}{\frac{s}{\omega_{LP}} + 1}$	1st order low-pass filter roll-off
$F_2(s)$	$\dfrac{1}{(\frac{s}{\omega_{LP}})^2 + 2\xi_{LP}\frac{s}{\omega_{LP}} + 1}$	2nd order low-pass filter roll-off
$F_3(s)$	$\dfrac{\frac{s}{\omega_n} + 1}{\frac{s}{\omega_d} + 1}$	1st order filter phase lead or lag
$F_4(s)$	$\dfrac{(\frac{s}{\omega_n})^2 + 2\xi_n\frac{s}{\omega_n} + 1}{(\frac{s}{\omega_d})^2 + 2\xi_d\frac{s}{\omega_d} + 1}$	2nd order filter phase lead or lag
$F_5(s)$	$\dfrac{(\frac{s}{\omega_d})^2 + 1}{(\frac{s}{\omega_d})^2 + 2\xi_d\frac{s}{\omega_d} + 1}$	Notch filter band stop
$F_6(s)$	$\dfrac{(\frac{s}{\omega_{a1}})^2 - 2\xi_{a1}\frac{s}{\omega_{a1}} + 1}{(\frac{s}{\omega_{a2}})^2 + 2\xi_{a2}\frac{s}{\omega_{a2}} + 1}$	All pass filters phase shifting

(from 10 to 35 parameters) to be selected Wei (2015). Thus, using an optimization routine is justified to find the best parameter combination.

2.1 Mathematical modeling

First, it is important to note that the primary focus of this paper is not on the modeling of the AMB–rotor system, and thus, the modeling presented here is discussed at a general level. To evaluate the optimization, a MIMO model of the flexible rotor is used. This model can be expressed in state–space form as follows:

$$\begin{aligned} \dot{\mathbf{x}}_{\mathrm{r}}(t) &= \mathbf{A}_{\mathrm{r}}\mathbf{x}_{\mathrm{r}}(t) + \mathbf{B}_{\mathrm{r}}\mathbf{u}(t), \\ \mathbf{y}_{\mathrm{r}}(t) &= \mathbf{C}_{\mathrm{r}}\mathbf{x}_{\mathrm{r}}(t) + \mathbf{D}_{\mathrm{r}}\mathbf{u}(t), \end{aligned} \qquad (2)$$

where $\mathbf{x}_{\mathrm{r}}$ is the state vector that contains both the modal position $\mathbf{q}_{\mathrm{m}}$ and the speed vectors $\dot{\mathbf{q}}_{\mathrm{m}}$. The input vector $\mathbf{u}$ represents the control currents (denoted by i_c) and the output vector $\mathbf{y}$ represents the xy plane displacements measured at the DE and NDE ends. These vectors are here defined as

$$\begin{aligned} \mathbf{x}_{\mathrm{r}} &= \begin{bmatrix} \mathbf{q}_{\mathrm{m}} \\ \dot{\mathbf{q}}_{\mathrm{m}} \end{bmatrix}, \\ \mathbf{u} &= \begin{bmatrix} i_{\mathrm{c},x,de} & i_{\mathrm{c},y,de} & i_{\mathrm{c},x,nde} & i_{\mathrm{c},y,nde} \end{bmatrix}^{\mathrm{T}}, \\ \mathbf{y}_{\mathrm{r}} &= \begin{bmatrix} x_{de} & y_{de} & x_{nde} & y_{nde} \end{bmatrix}^{\mathrm{T}}. \end{aligned} \qquad (3)$$

The state–space matrices of the AMB–rotor model are formed as follows Jaatinen et al. (2019)

$$
\mathbf{A}_r = \begin{bmatrix} \mathbf{0} & \mathbf{I} \\ (-\mathbf{M}_m^{-1})(\mathbf{K}_m + \mathbf{K}_{x,m}) & (-\mathbf{M}_m^{-1})(\mathbf{D}_m + \Omega\mathbf{G}_m) \end{bmatrix},
$$
$$
\mathbf{B}_r = \begin{bmatrix} \mathbf{0} \\ (-\mathbf{M}_m^{-1})\mathbf{K}_{i,m} \end{bmatrix}, \ \mathbf{C}_r = \begin{bmatrix} \mathbf{S}_S\tilde{\boldsymbol{\Phi}} & \mathbf{0} \end{bmatrix}, \ \mathbf{D}_r = \mathbf{0}.
$$

(4)

where $\mathbf{M}_m$ is the mass matrix, $\mathbf{D}_m$ is the damping matrix, $\mathbf{K}_m$ is the stiffness matrix, $\mathbf{G}_m$ is the gyroscopic matrix, Ω is the rotational velocity, $\mathbf{K}_{x,m}$ is the position stiffness, $\mathbf{S}_S$ is the transformation matrix and $\mathbf{K}_{i,m}$ represents the current stiffness. More detailed descriptions of the model and its parameters can be found in Nevaranta et al. (2023). To continue the modeling process, a simplified actuator model is derived by approximating the inner closed-loop control loop as a bandwidth approximation

$$
G_a(s) = \frac{\omega_{\text{bw}}}{s + \omega_{\text{bw}}}
$$

(5)

where $G_a(s)$ is the transfer function of the inner closed loop, and ω_{bw} represents the bandwidth of the PI-type current controller. In the full-system modeling, this is considered a block diagonal expression $blkdiag[G_a(s), G_a(s), G_a(s), G_a(s)]$. To ensure proper damping production with the correct phase condition of the controller, it is essential to incorporate lag-causing elements in the modeling of the AMB–rotor system. Thus, here a loop delay model is obtained using a Padé approximation represented with a 120 μs time delay. This represents the overall loop delay caused by various components. The complete system model used in the optimization problem is a combination of the rotor model with the three first flexible modes, the AMB and actuator model and the delay model.

2.2 Manual tuning of the controller using the Nyquist curve

In general, an effective AMB controller must ensure the robust stability and performance of the closed-loop system while guaranteeing damping conditions. Tuning controllers manually for rotor systems suspended by AMBs can be a challenging task, given the complex dynamics of the system. Nevertheless, specific tuning principles can be derived, as demonstrated in Lantto (1999), to facilitate the manual control design process, particularly in the case of sub-critical and low gyroscopic machines. The method proposed in Lantto (1999) uses controller loop shaping, employing a Nyquist curve with designated forbidden sensitivity regions. These regions specify where the curve,

or more specifically, the numerical ranges representing uncertainty, should not intersect. In this approach, the rotor model is constrained to be diagonal, allowing the derivation of a SISO controller tuning principle for the coupled MIMO system.

In this paper, the same framework is employed, but its visualization is enhanced through the introduction of disk margin metrics. The main idea of the original approach can be clarified by examining the SISO tuning case, focusing on the template illustrated in Fig. 2. In this depiction, the forbidden sensitivity area is delineated by a light blue circle centered at -1, with a radius of $\frac{1}{M_s}$, where M_s denotes the peak value of the sensitivity function $S(s)$. Here, $M_s = 2$ is considered, resulting in a circle with a radius of 0.5. Conversely, the forbidden region based on the complementary sensitivity function $T(s)$ is depicted by a yellow circle, positioned at $-\frac{M_t^2}{M_t^2-1}$ with a radius of $\frac{M_t}{|M_t^2-1|}$. When $M_t = 2$, a circle is centered at -4/3, with a radius of 2/3. As proposed in Lantto (1999), the second circle is defined by shifting the center of the complementary sensitivity circle to -2, based on practical experience. Finally, to ensure that the sensitivity function remains below 2 even with a 50 % increase in loop gain, a third circle can be drawn. This circle is represented by a yellow circle centered at -2/3, with a radius of 1/3. By combining these yellow circles, an overall template representing the forbidden regions is obtained, as shown in Fig. 2, and it can be used to guide the controller design. To be more specific, in Fig. 2, a simplified example using a rigid point mass model illustrates how adjustments in the parameters of a PID control combined with a second-order low-pass filter can impact the Nyquist curve $L(s) = C(s) \cdot G(s)$, either bringing it closer to or farther away from the forbidden region. The knowledge of how a single parameter impacts the curve facilitates the manual tuning process for PID-like controllers, particularly in low-frequency regions.

In this paper, the template serves a dual purpose: it is used for manual design of the initial controller, primarily aimed at ensuring that the controller has reasonable performance and stability. Additionally, it serves as a benchmark for assessing the results of optimization. To be more specific, in Section 3, this framework is used to evaluate the MIMO closed-loop system and compare the optimized controllers, and the approach based on numerical ranges Lantto (1999) is combined with forbidden regions to assess performance and stability in the low-frequency region, with a particular focus on the stability of the bending modes. This approach based on numerical ranges (representing input and output uncertainties) is used together with the forbidden regions to evaluate the performance/stability in the low-frequency region, but more importantly, also
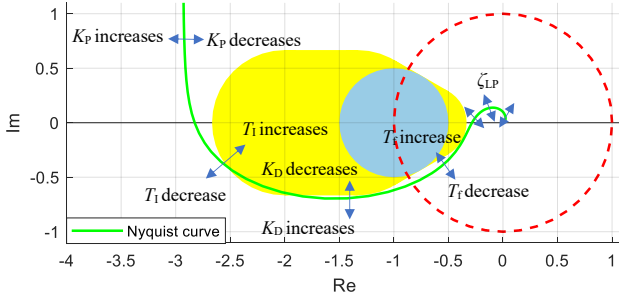
Figure 2: Example showing how a PID controller $C_{PID}(s)$ combined with a second-order low-pass filter $F_2(s)$ influences the movement of the Nyquist curve $L(s)$. The example involves SISO control applied to a rigid point mass system.

Figure 3: In the examined rotor configuration, the first three modes are characterized by free-free frequencies of 276 Hz, 605 Hz, and 950 Hz.

the stability and damping of the bending modes.

3 Optimization problem

This paper employs a Multiobjective Genetic Algorithm (MOGA) to obtain an optimal set of solutions (Pareto) for PID-based position controller parameters. The objectives are defined as minimizing the maximum sensitivity function value and maximizing the damping ratio in two distinct frequency ranges. To ensure the stability of the optimized controllers, a constraint is imposed on the eigenvalues and the parameter search space boundaries.

3.1 Defining MIMO optimization problem

Here, the generalized multiobjective optimization problem is formulated as minimizing/maximizing

$$\mathbf{y} = \left[f_1(\mathbf{x}), f_2(\mathbf{x}), \dots f_l(\mathbf{x}) \right]^T \qquad (6)$$

with a number of l objectives f_l subject to constraints

$$\mathbf{g} = \left[g_1(\mathbf{x}), g_2(\mathbf{x}), \dots, g_m(\mathbf{x}) \right]^T \leq \mathbf{0} \qquad (7)$$

The primary objective is to maximize the singular value of the sensitivity function, denoted by $\sigma(S)$. This singular value is defined as the larger of the maximal singular values associated with the driven end (DE) and the nondriven end (NDE), and as an objective as follows

$$f_1 = \sigma(S) = \max\{\sigma(S_{de}), \sigma(S_{nde})\}. \qquad (8)$$

The damping ratios of the eigenvalues are assessed separately within two frequency regions. This selection is naturally based on rotor dynamics and flexible mode
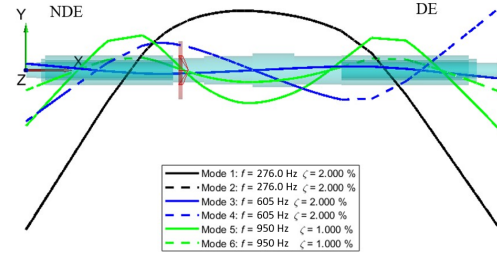
frequencies. Here, the first frequency region, containing the rigid and the first bending modes, spans from 0 to 300 Hz, while the second region ranges from 300 to 1000 Hz including the higher frequencies. Thus, these regions can be treated as individual objectives (f_2 and f_3, respectively) Wei and Söffker (2016) and can be defined as

$$f_2 = \xi_{\text{inv}[0\ 300]} = \frac{1}{\min(\xi_i)}, \quad \text{for} \quad i = 1 : k \qquad (9)$$

$$f_3 = \xi_{\text{inv}[300\ 1000]} = \frac{1}{\min(\xi_j)}, \quad \text{for} \quad j = 1 : m \qquad (10)$$

where ξ_i and ξ_j represent the damping ratio of the ith and jth eigenvalues, and k and m are the number of eigenvalues in the first and second frequency region, respectively. These objective functions are used to design the desired damping properties for different frequency regions. To guarantee that the outcome of the optimization problem is a stable control solution, the following constraint is considered as a closed-loop stability requirement

$$d = 0 - \max\{(Re(\lambda_n)\}, \text{ for } n = 1 : l, \qquad (11)$$

where $Re(\lambda_n)$ denotes the real value of the nth eigenvalue with a number of l eigenvalues.

The rotor configuration with the free-free modes is depicted in Fig. 3. Based on the selection criteria for both sides, the controllers consist of a combination of the PID control, second-order lead–lag filters, and second-order low-pass filters. The integrator time constants are excluded from the optimization problem, and it has a constant value of $T_I = 0.25$ s. Hence, the optimization involves 18 parameters in total. The objectives of the optimization are to minimize the maximum sensitivity value and increase damping in both the low- and high-frequency regions. In the low-frequency region, which includes the 1st bending mode
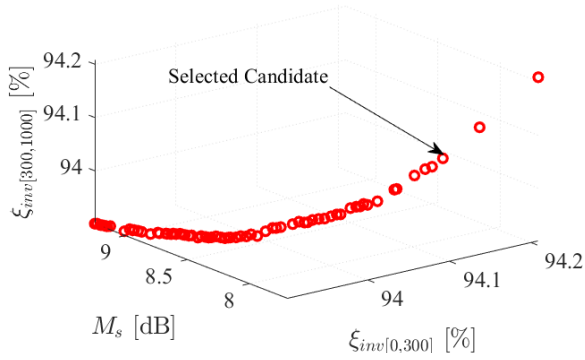
Figure 4: Pareto front plot obtained from the MOGA optimization; objective 1 represents the maximum sensitivity value (dB), while objectives 2 and 3 are the inverse damping ratios (%) in the frequency ranges of 0–300 Hz and 300–1000 Hz, respectively.
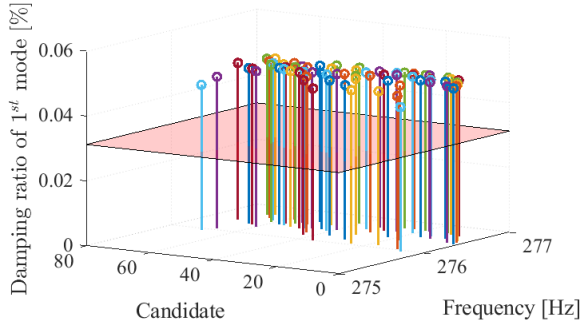

Figure 5: Stem plot of the damping ratio of the optimized candidates. The plane represents the initial damping near the first bending mode.

frequency, our goal is to increase the damping of the 1st bending mode and keep the damping below 5% for the 2nd and 3rd bending modes. Hence, the optimized controller should minimize the maximum value of the sensitivity function, enhance the damping ratio of the 1st bending mode (at 276 Hz), and produce positive (low) damping in the high-frequency region (300–1000 Hz) to stabilize the closed-loop control.

3.2 Optimization results

For the example case studied in this paper, the initial controller (manually tuned) was intentionally designed with a low damping for the first mode and a higher output sensitivity at the DE channel. To be more specific, the maximum value of the output sensitivity function $S_{de}(s)$ is 13 dB, and the damping ratio of the 1st bending mode frequency is 3%. The multiobjective optimization algorithm employed here is the non-dominated sorting genetic algorithm (NSGA–II), with
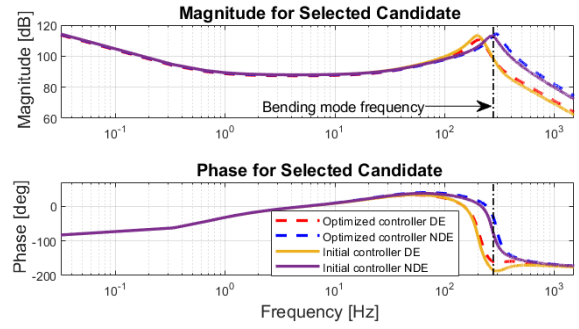

Figure 6: Frequency response plots of the initial and selected controller candidates (optimized).

a population size of 200. For the optimization problem, a 10% variation of the manually tuned controller parameters was considered for both the lower and upper bounds where Wei (2015) considered 20% . A total of 70 candidates (Pareto) optimal solutions were obtained as shown in Fig. 4, expressed as a function of objectives. The selected candidate, depicted in Fig. 4, was chosen from the set of Pareto solutions based on engineering judgement, and the corresponding optimized parameters are provided in Table 2. The best candidate was selected based on having the minimum sensitivity function value and high damping in the frequency region of the first bending mode. However, in general, choosing a candidate from the Pareto set that fully satisfies all objectives is not always straightforward owing to the trade-offs between them Villarreal-Cervantes (2017). For example, selecting a candidate with a high damping gain may simultaneously increase the maximum value of the sensitivity function. This trade-off is evident in the observed behavior; all of the 70 optimal candidates displayed increased damping close to the frequency of the first bending mode, as demonstrated in Fig. 5. When further considering the damping condition, Fig. 6 illustrates the frequency responses of both controllers with the initial controller parameters and the optimized parameters. The initial damping ratio at the first bending mode frequency (276 Hz) was 3%, and as can be seen in Fig. 5, it is increased to 5%. This is evident from the controller phase condition shown in Fig. 6 as its shape on the DE side has changed, indicating a change in the damping properties.

A further analysis of the robustness and performance of the initial and optimized closed-loop controllers was carried out using a numerical-range-based generalized Nyquist curve depicted in Fig. 8. It is noteworthy that the original visualization illustrated in Fig. 2 is simplified by considering only the blue and yellow cir-

Table 2: Nominal and optimized DE- and NDE-side controller parameters considered in the optimization problem with the search space expressed as lower and upper bounds.

Parameter (DE)	K_P	K_d	T_f	ω_{LP}	ξ_{LP}	ω_n	ξ_n	ω_d	ξ_d
Nominal	25000	100	0.0010	1257	0.13	1979	0.30	1508	0.30
Upper bound	27500	110	0.0011	1382	0.14	2180	0.33	1659	0.33
Lower bound	22500	90	0.0009	1131	0.12	1784	0.27	1357	0.27
Optimized	23116	94	0.0010	1335	0.12	1922	0.32	1608	0.29
Parameter (NDE)	K_P	K_d	T_f	ω_{LP}	ξ_{LP}	ω_n	ξ_n	ω_d	ξ_d
Nominal	25000	100	0.0010	1697	0.12	1005	0.25	1351	0.60
Upper bound	27500	110	0.0011	1867	0.13	1106	0.28	1486	0.66
Lower bound	22500	90	0.0009	1527	0.11	905	0.23	1216	0.54
Optimized	23408	95	0.0009	1838	0.11	989	0.23	1360	0.59

cles representing the complementary sensitivity function and output sensitivity. However, the visualization is simultaneously enhanced by incorporating the concept that the multi-loop disk margin Seiler et al. (2020) represents the largest region for simultaneous and independent variations for individual output channels of a loop transfer function. Thus, the red solid circle inside the blue output sensitivity region indicates the MIMO disk phase margin. The MIMO system is evaluated by considering the uncertainty in the stiffness properties of the AMB (represented by the matrix $\mathbf{\Delta}_{in}$ with a 10% deviation from the nominal values) and sensor sensitivity (represented by the matrix $\mathbf{\Delta}_{out}$ with a 10% deviation from nominal values) depicted in Fig. 8 as numerical ranges of the matrix $\mathbf{L}(s) = \mathbf{\Delta}_{in}\mathbf{C}(s)\mathbf{G}(s)\mathbf{\Delta}_{out}$ evaluated at different frequencies. Further, in the figure, the curves $L(s)_{DE}$ and $L(s)_{NDE}$ represent the DE- and NDE-side SISO Nyquist curves, respectively.

Comparing the results of the initial controller (depicted in Fig. 8(a)) with the optimized controller (Fig. 8(b)), it is observed that the optimized controller is shifting the numerical ranges (curves) further away from the forbidden output sensitivity region at low frequencies. This shift results in an increase in the robustness (stability and performance) of the system, which is evident from the enlargement of the red circle indicating the disk phase margin. The original disk phase margin was 4.9°, and with the optimized controller, it increased to 12.4°. Close to the first bending mode, the initial controller performs similarly, as we can see from Fig. 8 that the numerical ranges evaluated close to the bending mode frequency (263–303 Hz) are not violating the defined regions. Furthermore, near the second and third bending mode frequencies, no significant difference is observed between the initial and optimized controllers from the curve as the numerical ranges are far away from the forbidden region in both cases.
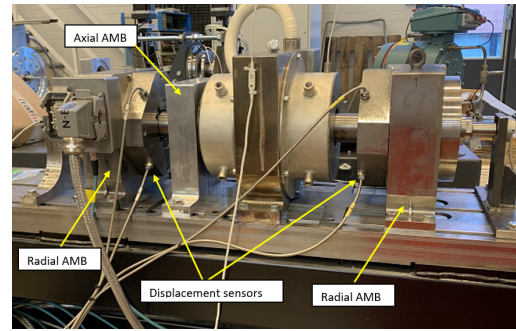

Figure 7: Experimental test system consisting of two radial and one axial magnetic bearings.

4 Experimental Results

The experimental test system was used to validate the optimization results both in the time and frequency domains. The system is illustrated in Fig. 7, and it incorporates two radial AMBs and one axial AMB to stabilize the rotor movement. The AMBs are controlled amplifiers, and an industrial PC (Beckhoff, TwinCat) is employed for implementing the control software and data acquisition. The rotor displacement is measured in four radial and one axial directions using eddy current sensors manufactured by Bentley Nevada.

Initially, the output sensitivity functions were experimentally identified using the initial and optimized controllers with the AMB–rotor system at levitation (zero speed). This was achieved by superposing a stepped sine excitation signal to the PID controller output, one channel and one frequency at a time, using a signal with an amplitude of 0.2 A and frequencies ranging from 1 Hz to 1000 Hz with a 1 Hz resolution. As mentioned above, the DE-side manually tuned controller was intentionally designed with a poor stability/performance, and thus, the measured sensitivity of the initial controller is above the A/B zone of 9.54 dB, while the optimized controller reduces the maxi-
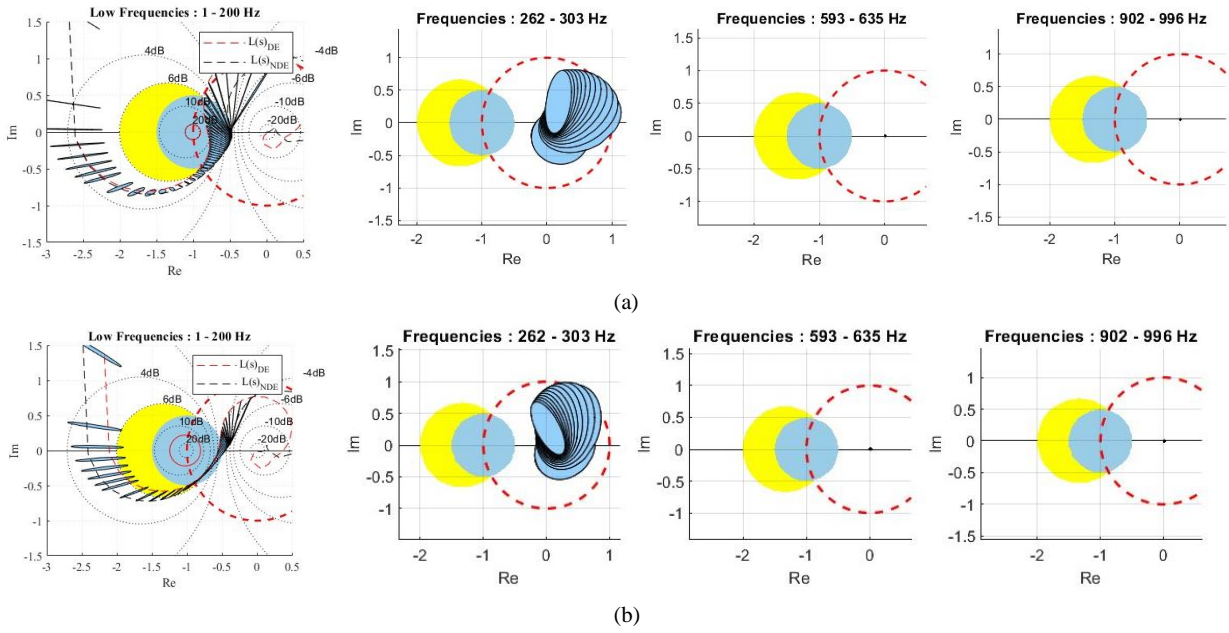
Figure 8: Generalized Nyquist diagram $\mathbf{L}(s)$ for (a) initial control parameters tuned intentionally with a poor-performing DE channel (red dashed line) and (b) optimized control parameters. In the low-frequency region, the numerical ranges are evaluated from 1 to 200 Hz, while at the bending mode frequencies, consideration is given to frequencies near the bending mode frequency. On the left, the red solid circle inside the blue output sensitivity region indicates the MIMO disk phase margin.
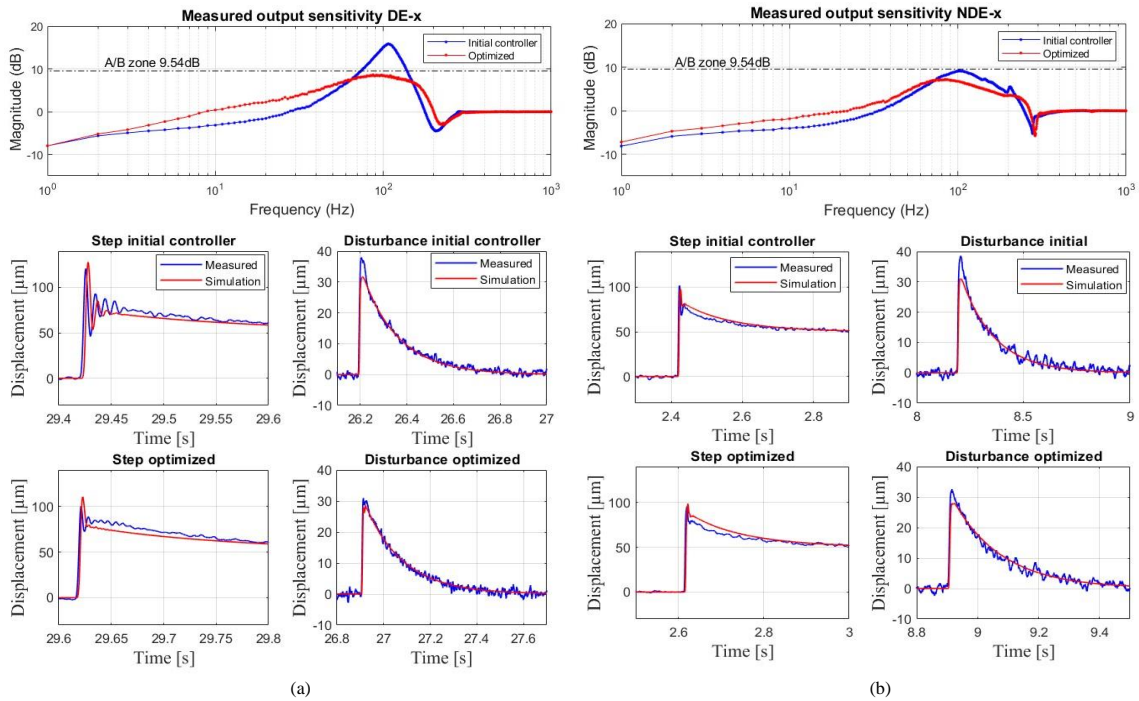

Figure 9: Experimentally identified output sensitivities (above), position step response and current disturbance step response using the initial and optimized controllers; (a) driven end (DE), x-position and (b) nondriven end (NDE) x-position.

mum sensitivity value below the A/B zone as shown in Fig.9(a). Similarly, the NDE-side initial controller in Fig.9(b) is close to the A/B zone limit. However, after optimization, the sensitivity is close to 7 dB, indicating that the optimized controller improves the performance and robustness. Moreover, for time-domain validation, a step input of 50 μm was applied to the position reference, and an input current step of 0.2 A was injected into the controller output. The measured step response with the initial and optimized DE- and NDE-side controllers is depicted in Figs. 9(a) and (b). As it can be seen from the plot, the measured optimized controller reduced the overshoot from the DE side approximately by 120 μm to 100 μm, and at the same time, the disturbance step amplitude was reduced. Thus, both the frequency-domain and time-domain validation clearly demonstrate that the optimization of the control parameters results in improved system stability and performance, which is in agreement with the results observed in the Nyquist plots.

5 Conclusions

This paper introduced an optimization approach for PID-based controllers used in AMB–rotor systems. The method is based on a Multiobjective Genetic Algorithm (MOGA) with two objectives and additional constraints to guarantee stable closed-loop solutions. The approach is integrated into a visualization framework using Nyquist diagrams combined with disk margin and damping ratio plots to validate the achieved robustness and performance. Experimental validation demonstrated that the optimization produces effective controllers, achieving the desired properties when evaluated in both the time and frequency domains. While the proposed approach optimized the damping of the first mode, more complex cases, such as gyroscopic machines, require additional damping objectives for specific frequency regions. Consequently, this increases the number of filter components and controller parameters, but when evaluated against the framework considered here, the reasonableness of the controller is straightforward to evaluate.

Acknowledgments

References

Agees Kumar, C. and Kesavan Nair, N. Multiobjective pi controller design with an application to speed control of permanent magnet dc motor drives. In *2011 International Conference on Signal Processing, Communication, Computing and Networking Technologies*. pages 424–429, 2011. doi:10.1109/ICSCCN.2011.6024588.

Gaidhane, P. J., Kumar, A., and Nigam, M. J. Tuning of two-dof-fopid controller for magnetic levitation system: A multi-objective optimization approach. In *2017 6th International Conference on Computer Applications In Electrical Engineering-Recent Advances (CERA)*. pages 479–484, 2017. doi:10.1109/CERA.2017.8343377.

Hutterer, M., Hofer, M., and Schrödl, M. Decoupled control of an active magnetic bearing system for a high gyroscopic rotor. In *2015 IEEE Int. Conf. on Mechatronics (ICM)*. pages 210–215, 2015. doi:10.1109/ICMECH.2015.7083976.

Hutterer, M. and Schroedl, M. Stabilization of active magnetic bearing systems in the case of defective sensors. *IEEE/ASME Transactions on Mechatronics*, 2022. 27(5):3672–3682. doi:10.1109/TMECH.2021.3131224.

Hutterer, M. and Schrödl, M. Modeling and mu-synthesis control of a flexible rotor stabilized by active magnetic bearings including current free control. *Journal of Sound and Vibration*, 2023. 546:117439. doi:https://doi.org/10.1016/j.jsv.2022.117439.

Jaatinen, P., Vuojolainen, J., Nevaranta, N., Jastrzebski, R., and Pyrhönen, O. Control System Commissioning of Fully Levitated Bearingless Machine. *Modeling, Identification and Control*, 2019. 40(1):27–39. doi:10.4173/mic.2019.1.3.

Jastrzebski, R. P., Hynynen, K. M., and Smirnov, A. $h\infty$ control of active magnetic suspension. *Mechanical Systems and Signal Processing*, 2010. 24(4):995–1006. doi:https://doi.org/10.1016/j.ymssp.2009.10.008.

Jastrzebski, R. P., Kurvinen, E., and Pyrhönen, O. Design, modelling and control of mimo amb system with 3 radial bearing planes for megawatt-range high-speed rotor. In *2019 IEEE International Electric Machines & Drives Conference (IEMDC)*. pages 805–811, 2019. doi:10.1109/IEMDC.2019.8785378.

Lantto, E. *Robust Control of Magnetic Bearings in Subcritical Machines*. Ph.D. thesis, 1999.

Liu, B., Sjöberg, J., and Laiho, A. Optimization-based radial active magnetic bearing controller design and verification for flexible rotors. *Proceedings of the Institution of Mechanical Engineers, Part I: Journal of Systems and Control Engineering*, 2016. 230(4):339–351. doi:10.1177/0959651815621675.

Meng, L. and Xue, D. Design of an optimal fractional-order pid controller using multi-objective ga optimization. In *2009 Chinese Control and Decision Conference*. pages 3849–3853, 2009. doi:10.1109/CCDC.2009.5191796.

Nevaranta, N., Jaatinen, P., Vuojolainen, J., Sillanpää, T., and Pyrhönen, O. Adaptive mimo pole placement control for commissioning of a rotor system with active magnetic bearings. *Mechatronics*, 2020. 65:102313. doi:https://doi.org/10.1016/j.mechatronics.2019.102313.

Nevaranta, N., Shishkov, A., Abubakar, I., Putkonen, A., Rehtla, M., Ranjan, G., and Lindh, T. Neural networks for data-driven modeling of active magnetic bearing suspended rotor system. In *2023 IEEE 6th Student Conference on Electric Machines and Systems (SCEMS)*. pages 1–6, 2023. doi:10.1109/SCEMS60579.2023.10379332.

Noshadi, A., Shi, J., Lee, W. S., Shi, P., and Kalam, A. System identification and robust control of multi-input multi-output active magnetic bearing systems. *IEEE Transactions on Control Systems Technology*, 2016. 24(4):1227–1239. doi:10.1109/TCST.2015.2480009.

Polajzer, B., Ritonja, J., Stumberger, G., Dolinar, D., and Lecointe, J.-P. Decentralized pi/pd position control for active magnetic bearings. *Electrical Engineering*, 2016. 89(1):53–59. doi:10.1007/s00202-005-0315-1.

Sahinkaya, A. and Sawicki, J. T. Computationally efficient implementation of robust controllers in active magnetic bearing systems. *Mechanical Systems and Signal Processing*, 2020. 144:106902. doi:https://doi.org/10.1016/j.ymssp.2020.106902.

Schmied, J. and Kosenkov, A. Practical controller design for rotors on magnetic bearings by means of an efficient simulation tool. volume Volume 7B: Structures and Dynamics of *Turbo Expo: Power for Land, Sea, and Air*. 2013. doi:10.1115/GT2013-95075. V07BT30A021.

Seiler, P., Packard, A., and Gahinet, P. An introduction to disk margins [lecture notes]. *IEEE Control Systems Magazine*, 2020. 40(5):78–95. doi:10.1109/MCS.2020.3005277.

Villarreal-Cervantes, M. Approximate and widespread pareto solutions in the structure-control design of mechatronic systems. *J Optim Theory Appl*, 2017. 173:628–657. doi:10.1007/s10957-016-1053-4.

Wei, C. Controller design and optimization for rotor system supported by active magnetic bearings. 2015. URL https://api.semanticscholar.org/CorpusID:191554570.

Wei, C. and Söffker, D. Improving pid-control of amb rotor system design i: Optimization strategy. In *13th Int. Symp. on Magnetic Bearings 2012*. pages 1–15, 2012a.

Wei, C. and Söffker, D. Improving pid-control of amb rotor system design ii: Experimental results. In *13th Int. Symp. on Magnetic Bearings 2012*. pages 1–8, 2012b.

Wei, C. and Söffker, D. Optimization strategy for pid-controller design of amb rotor systems. *IEEE Transactions on Control Systems Technology*, 2016. 24(3):788–803. doi:10.1109/TCST.2015.2476780.

Zhang, S. Y., Wei, C. B., Li, J., and Wu, J. H. Robust h∞ controller based on multi-objective genetic algorithms for active magnetic bearing applied to cryogenic centrifugal compressor. In *2017 29th Chinese Control And Decision Conference (CCDC)*. pages 46–51, 2017. doi:10.1109/CCDC.2017.7978064.